

URTeC: 5668

Evaluation of Electron Tomography Reconstruction Methods for a Barnett Shale

Laura Frouté*, Emeric Boigné, Matthias Ihme, Anthony R. Kavscek, Stanford University.

Copyright 2021, Unconventional Resources Technology Conference (URTeC) DOI 10.15530/urtec-2021-5668

This paper was prepared for presentation at the Unconventional Resources Technology Conference held in Houston, Texas, USA, 26-28 July 2021.

The URTeC Technical Program Committee accepted this presentation on the basis of information contained in an abstract submitted by the author(s). The contents of this paper have not been reviewed by URTeC and URTeC does not warrant the accuracy, reliability, or timeliness of any information herein. All information is the responsibility of, and, is subject to corrections by the author(s). Any person or entity that relies on any information obtained from this paper does so at their own risk. The information herein does not necessarily reflect any position of URTeC. Any reproduction, distribution, or storage of any part of this paper by anyone other than the author without the written consent of URTeC is prohibited.

Abstract

Electron tomography (ET) imaging provides nanometer-scale measurements of the structure of solid samples. ET, with an appropriate reconstruction workflow, provides significant insight into a variety of shale properties including structure, fluid transport and reaction. Despite the advantageous high resolution, the tomographic reconstruction of a three-dimensional (3D) structure from multiple 2D projections presents several challenges. In particular, because of the limited transmission of electrons through the sample, the signal to noise ratio remains small and the projection range is restricted to only a partial set of angles ($\pm 60^\circ$ tilt angle). This missing wedge of angles results in tomographic artifacts that deteriorate the quality of the reconstructed volume, thereby compromising the accurate characterization of the nanometer-scale network of pores. To address these challenges, this study evaluates quantitatively the capabilities of ET. This work sits at the intersection of two disciplines: unconventional reservoir evaluation and computational imaging. It is the first of its kind to offer a comparison of the robustness of ET reconstruction methods applied to a shale thin section. Specifically, the properties of an organic pore network are compared over different reconstruction algorithms. First, Fourier techniques (Weighted Back-Projection, Filtered Back-Projection) and iterative techniques (Conjugate Gradient Least Squares, Simultaneous Iterative Reconstruction Technique) are used to reconstruct the structure of a Barnett shale sample. The pore network inside of and around a region of organic matter is visualized in 3D. Comparisons between the different reconstruction methods highlight the variability observed in regions with small pores. This variability is then quantified by comparing values of storage and transport metrics over the different methods. Finally, synthetic numerical phantoms and model samples are used to illustrate the limitations of the method and quantify the effect of artifacts. It is found that a strong agreement is observed for large pores over the different ET reconstruction workflows considered while a wider variability exists for small features. As a result, even though ET can provide robust estimates of the porosity of shale samples, the accurate determination of connectivity and transport metrics remains challenging due to missing wedge artifacts and noise limitations. The results suggest that application of ET to such samples benefits from artifact-reduction techniques. Experimental reduction in the missing wedge, and advanced reconstruction methods that fill-in the missing information, represent promising opportunities to characterize more accurately pore network properties in shale samples.

Introduction

Today, there remains a significant lack of understanding of the nanometric pore networks within shale rocks. Evidence suggests that connected nanopores govern the flow of confined fluids from the organic matter to the fractures, therefore greatly influencing hydrocarbon recovery. But experimental measurements at the relevant scale remain scarce because many imaging techniques lack the resolution to observe individual nanopores. Thus, there is a growing need to develop advanced imaging methods to resolve shale nanoporosity to build a multiscale tool for the simulation of hydrocarbon transport (Striolo et al., 2017; Guo et al., 2018; Frouté et al., 2020).

With exceptional nanometer resolution, electron microscopy techniques alone offer the significant magnification needed to resolve shale nanoporosity (Loucks et al., 2012; Curtis et al., 2012; Bernard et al., 2013; Chen et al., 2015; Zhou et al., 2016; Berthonneau et al., 2017; Ma et al., 2018; Goral et al., 2019). In Scanning Transmission Electron Microscopy (STEM), the electron beam is focused to a fine spot that scans the sample in a rastering pattern, producing images with sub-nanometer pixel size. Depending on the detector, the measurement is either of the transmitted electrons (bright field imaging) or of the forward scattered electrons (dark field imaging). Specifically, High-Angle Annular Dark-Field (HAADF) detectors measure Rutherford electrons that scatter further than 3° from the centerline. This imaging modality is highly sensitive to changes in the atomic number Z of atoms in the sample. Thus, it is particularly appropriate to separate mineral, organic matter, and pores inside rocks. By collecting HAADF-STEM projections at incremental tilt angles, Electron Tomography (ET) reveals three-dimensional (3D) shale structures, with unparalleled nanometer resolution. A handful of recent studies have produced 3D representations of organic nanopores, described the pore network morphology, and highlighted the prevalent role of connected nanopores in hydrocarbon transport (Adler et al., 2020; Berthonneau et al., 2018; Ma et al., 2018). In an effort to reveal the 3D geometry and resulting flow properties of organic nanopore networks, HAADF-STEM tomography was employed to image Barnett shale samples (Frouté et al., 2020). It was found that the flow occurred primarily through networks with pores above 20 nm in diameter.

Even though smaller pores are clearly visible in the HAADF-STEM images, the limited tomographic reconstruction quality compromises the extraction of the smallest percolating pathways. Indeed, despite its advantageous resolution, ET imaging suffers from several limitations. In particular, ET is limited by the reduced penetration of electrons through solid samples that results in a small signal to noise ratio (SNR), and a limited tilt range (Acar et al., 2016; Messaoudil et al., 2007; Penczek, 2010; Paavolainen, 2014; Ercius, 2015). These limitations result in tomographic artifacts that deteriorate the quality of the reconstructed volume, thereby compromising the accurate characterization of the nanometer-scale network of pores. Because these limitations are also relevant in X-ray tomography, a large amount of research in medical and material sciences has focused on improving tomographic reconstruction and segmentation techniques. Specifically, different reconstruction methods with varying sets of parameters have been developed to improve the image quality in cases with limited signal and missing angular wedge. Depending on the method and parameters used, significant variations are observed in the reconstruction quality. However, in the context of rock nano-structures, only limited work has investigated the impact of the tomographic method on the reconstructed sample structure and properties. In fact, the precise characterization of shale nanostructures remains limited by the image quality post-reconstruction (Adler et al., 2020), thus making this comparative effort especially relevant.

To investigate the variability from ET imaging, the present study evaluates quantitatively the capabilities of HAADF-STEM tomography for shale applications. The accuracy of the 3D imaging of rock nanostructures is investigated by performing volumetric reconstructions of a Barnett shale tomographic dataset, and comparing different acquisition modalities and post-processing techniques. The variability observed is quantified by computing values of storage and transport metrics for the different methods. The dominant challenges imposed by the acquisition modalities are identified as the limited projection range and small SNR. To study their significance, we first compare data acquired with different projection ranges,

and different tilt angle increments, respectively. Next, an experimental phantom consisting of perfect spheres is used to illustrate the artifacts caused by ET limitations. The experimental dataset is compared with a numerical phantom, as frequently used in the tomography literature to highlight artifacts (Messaoudil et al., 2007). Finally, we consider data acquired with optimal settings and we evaluate the uncertainty of the two main post-acquisition processes: 3D reconstruction, and porosity segmentation. The 3D shale structures obtained by four different reconstruction techniques are compared thoroughly.

Methods

Scanning Transmission Electron Microscopy (STEM) is based on the transmission of a beam of electrons through relatively thin samples. Roughly 100 nm thick sections (i.e., lamellae) are needed to produce volumetric projections with nanometer resolution. A clay-rich, siliceous, and mature shale sample from the Barnett formation (8635 ft) was selected for this study. A subsample was cut from the Barnett plug parallel to bedding, polished, and mounted for electron microscopy. A shale lamella was prepared by FIB-SEM milling (see Fig. 1.a.). We acquired STEM tomograms of the lamella at high magnification in High-Angle Annular Dark-Field imaging mode (HAADF). The tilt series, with pixel sizes of 1.24nm, was collected by rotating the thin section to $\pm 60^\circ$ from the horizontal, with 1° increments. ET acquisitions were carried out with a state-of-the-art transmission electron microscope (FEI Titan 80-300), under a 300kV accelerating voltage, and assisted by the Xplore3D software (ThermoFisher Scientific).

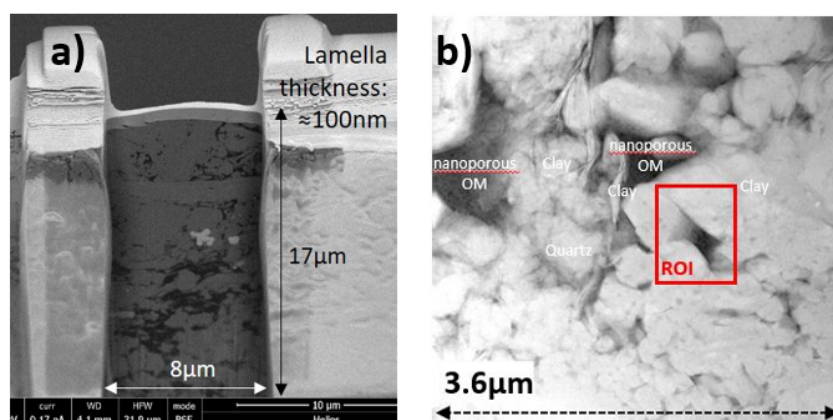


Figure 1. a) TEM lamella preparation of a Barnett shale sample by FIB-SEM. b) 2D STEM image showing the location of the ROI

Alignment, image processing, 3D reconstruction and segmentation was needed to extract quantitative information from image datasets. Stage shifts and tilt series misalignments were corrected using Inspect3D (Version 3.0, ThermoFisher Scientific). A stack of parallel slices was then reconstructed using four different standard tomographic algorithms. The first two techniques are direct methods that use the Fourier properties of the Radon transform to compute its inverse using FFTs. Specifically, we used the Weighted Back-Projection (WBP) implementation from TomoJ (Version 2.6, plug-in for ImageJ, public domain), and the Filtered Back-Projection (FBP) from the ASTRA Toolbox (Van Aarle et al., 2016). The latter two techniques are iterative reconstruction techniques that minimize a least-square data-fidelity term: the Simultaneous Iterative Reconstruction Technique (SIRT) and the Conjugate Gradient Least Squares (CGLS). The GPU-accelerated implementations from the ASTRA Toolbox were used with 7 iterations for CGLS, and 60 iterations for SIRT. Note that for all methods, the reconstruction was performed directly on the pixel intensity images, without any correction of the contrast transfer function (Penczek, 2010).

Using TomoJ, the stack was resliced in the Z direction, aligned horizontally, and filtered. A sub-volume was extracted to focus on a region of interest (ROI) containing nano-porous organic matter. Figure 1b) shows the location of the ROI in the sample. The images were then segmented using the machine

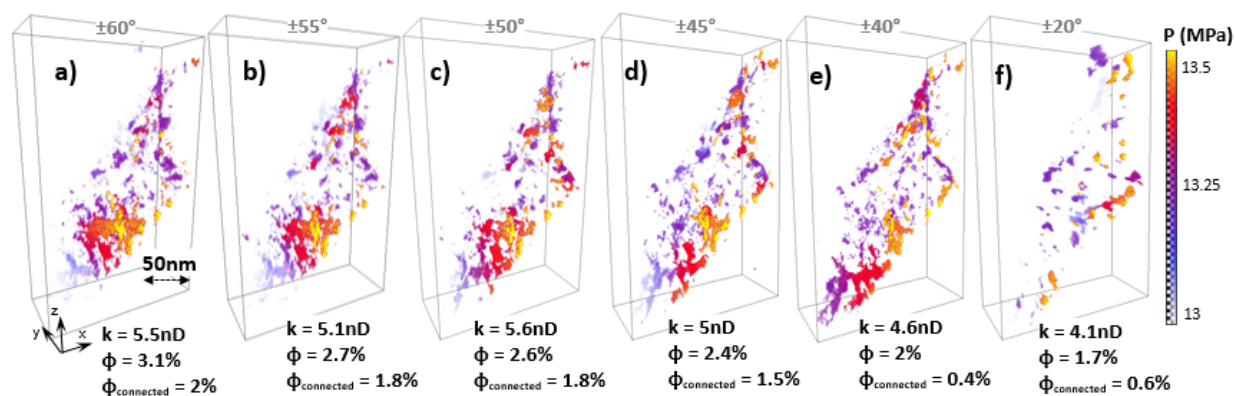


Figure 3. Pressure maps obtained on pore networks reconstructed with the FBP technique from reduced angle ranges (a: $\pm 60^\circ$, b: $\pm 55^\circ$, c: $\pm 50^\circ$, d: $\pm 45^\circ$, e: $\pm 40^\circ$, f: $\pm 20^\circ$).

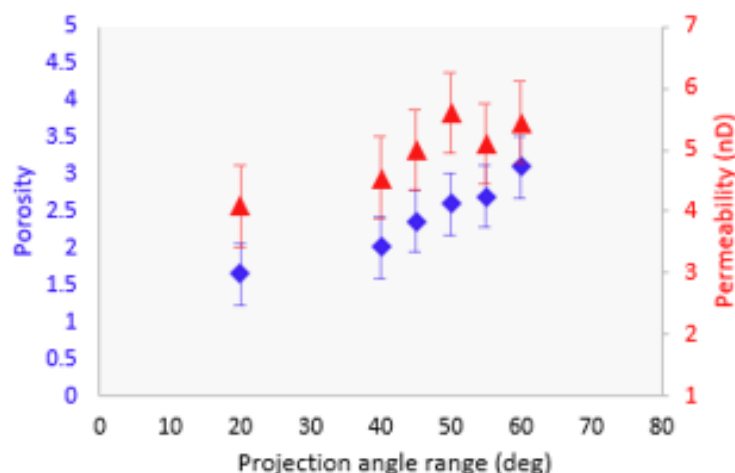


Figure 4. Increase in porosity (blue) and permeability (red) as the projection angle range improves.

SNR limitations

The greater the number of images acquired during tomography, the larger the cumulative electron count and the greater the SNR. Small SNR deteriorates the quality of the reconstructed volume by increasing the amount of high spatial frequency noise within the 3D dataset. This high-frequency noise is particularly detrimental to the porous network extraction, as it becomes challenging to identify whether adjacent pores are connected. Low-pass filtering can be applied *a posteriori* to reduce this high-frequency noise, but it comes at the cost of a loss in spatial resolution. To further evaluate the impact of SNR on the porous network extraction, we performed different FBP reconstructions of our dataset, first with the original 1° tilt sampling (121 images), and then with reduced sampling (61 images with 2° increment and 41 images with 3° increment). The loss of information from skipping adjacent angles is minimal, thus making this approach appropriate to highlight the impact of SNR.

After extracting the pore space, we conducted numerical flow experiments across the XZ planes, in the Y direction. The resulting pressure maps are presented in Fig. 5. They confirm that small SNR significantly degrades the 3D pore extraction. The decrease in porosity and permeability as a function of the angular resolution is captured in Fig. 6. We note an abrupt decrease in porosity and permeability as the angular increment increases. The loss of information in datasets with high angular increments results in heavily fragmented porous networks that fail to capture the main flow paths. This observation is consistent with the increase in high-frequency noise and the loss of pore connectivity.

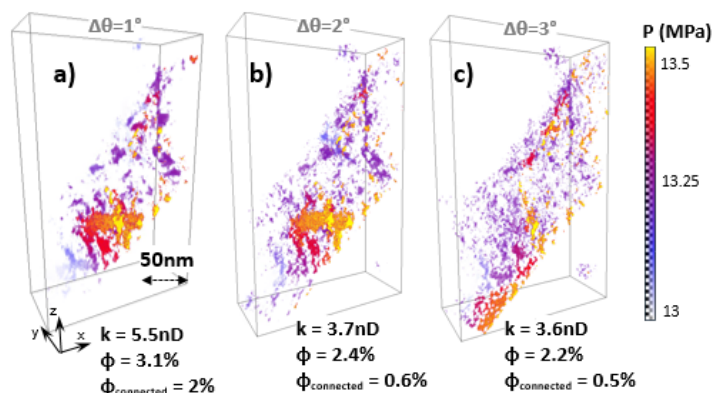


Figure 5. Pressure maps obtained on pore networks reconstructed with the FBP technique with varying tilt increments (a: 1°, b: 2°, c: 3°).

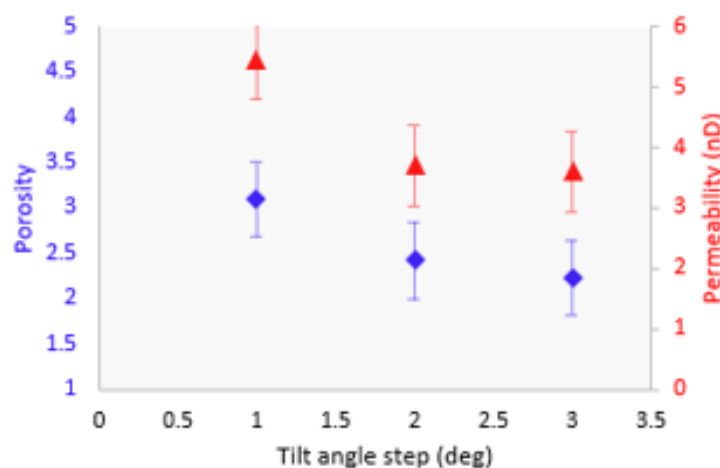


Figure 6. Decrease in porosity (blue) and permeability (red) as the angular resolution worsens.

Analyzing artifacts using numerical phantoms

Numerical phantoms are commonly used in tomography to optimize the reconstruction method and improve the quality of the 3D dataset. To highlight the tomographic artifacts resulting from the missing angle wedge, we used gold-shadowed latex beads (#628-B, Pelco) that are 204 nm in diameter. Because the latex beads are perfect spheres, any deviation from sphericity during the reconstruction is caused by tomographic artifacts. Figure 7 shows the STEM projection acquired at 0° of the latex beads. Visible are eight gold-shadowed latex beads, surrounded by a lattice work of evaporated gold (in white). In the XZ plane, clear losses in the bead sphericity are visible.

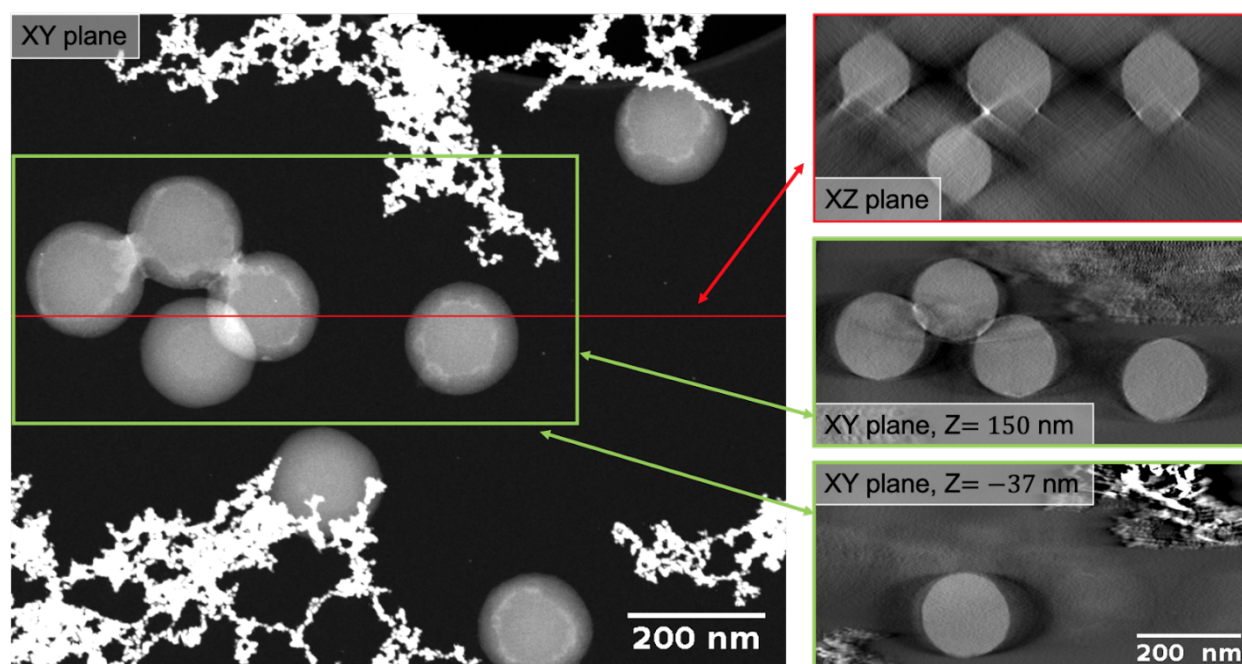


Figure 7. Reconstructions using the FBP algorithm of a real dataset of beads acquired over the angular range $\pm 60^\circ$ along the y-axis. The left image is the raw HAADF-STEM image acquired at 0° , while the right three images show cross-sections after ET reconstruction. The top-right image shows a cross-section along the XZ plane indicated in red, clearly highlighting missing-wedge artifacts. The two other images are cross-sections acquired at different depths Z, revealing the separation of the overlapped beads in the left image.

To investigate these artifacts, a numerical 3D phantom consisting of four beads was constructed, and a dataset of 2D projection images was numerically computed. This phantom dataset was then reconstructed similarly as the experimental data using the FBP algorithm. The effect of acquiring angles over the limited range only ($\pm 60^\circ$), instead of the ideal angle range ($\pm 90^\circ$), is presented in Fig. 8. These results clearly highlight that the loss of sphericity in the XZ plane shown in Fig. 7 is due to the missing wedge of angles. This result is consistent with tomographic sampling theory that highlights that the $0-180^\circ$ angular range is required for an exact 3D reconstruction.

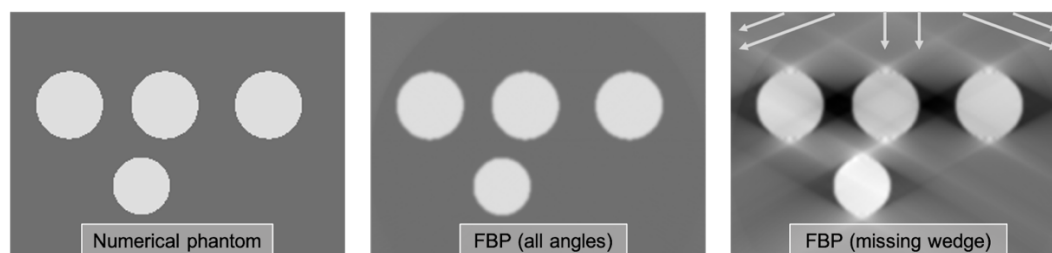


Figure 8. Reconstructions using the FBP algorithm of an ideal numerical phantom made of four spheres (left). Two reconstructions are reported using projection data acquired over (center) the entire $\pm 90^\circ$ angular range, and (right) only the $\pm 60^\circ$ range. For the missing wedge case, the angular range achieved is indicated with grey arrows. The angular increment used numerically is 1° .

Figure 9 shows a 3D reconstruction of the phantom, with three gold-shadowed spheres apparent in the foreground. Visible in the background is evaporated gold that forms meshes around the gold-coated latex particles. The results show that, despite the missing-wedge artifacts, the latex particles are reconstructed with a reasonably spherical shape using only a $\pm 60^\circ$ angle range. This result highlights that, although missing-wedge artifacts can be significant, ET remains a promising technique to resolve 3D structures at the nanometer scale.

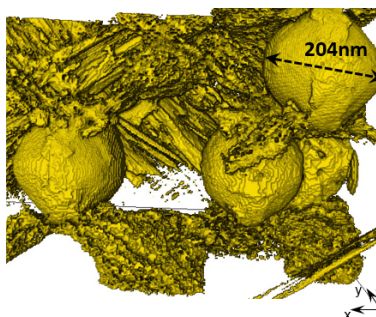


Figure 9. 3D reconstruction of the gold-shadowed latex particles in a lacework of evaporated gold.

ET Reconstruction

We now considered data acquired with optimal settings ($\pm 60^\circ$ projection range, 1° increments) to investigate the uncertainty of post-acquisition processes. To evaluate the impact of the reconstruction method on the image quality, 3D datasets reconstructed using different algorithms were compared. Figure 10 shows the ROI of the middle slice in the XZ and XY planes after reconstruction using the FBP, WBP, CGLS, and SIRT algorithms. The reconstructed nanopore structures appear very similar for the four different reconstruction techniques, but with some variations in the definition of the grain edges and pores. Note that the FBP and WBP direct methods produce sharper and noisier images, whereas the SIRT and CGLS iterative methods produce blurrier images. This trend is expected given the inherent low-pass filtering behavior of the iterative methods when a small number of iterations is used.

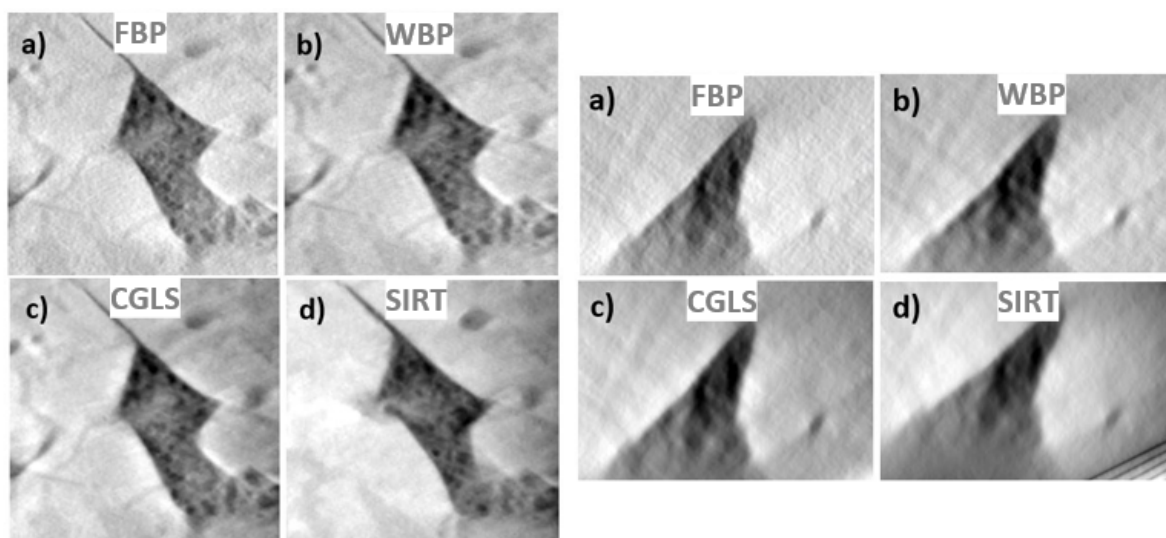


Figure 10. Left: XZ view of the ROI reconstructed with different techniques (a: FBP, b: WBP, c: CGLS, d: SIRT). Right: XY view of the ROI reconstructed with different techniques (a: FBP, b: WBP, c: CGLS, d: SIRT).

A representation of the extracted pore volumes is shown in Fig. 11. The four pore volumes have values of porosity between 2.6 and 3.4%. Fig. 11e) shows the porosity that is common to all reconstructions. A strong agreement is observed for large pores over the different ET reconstruction workflows while a wider variability exists for small features.

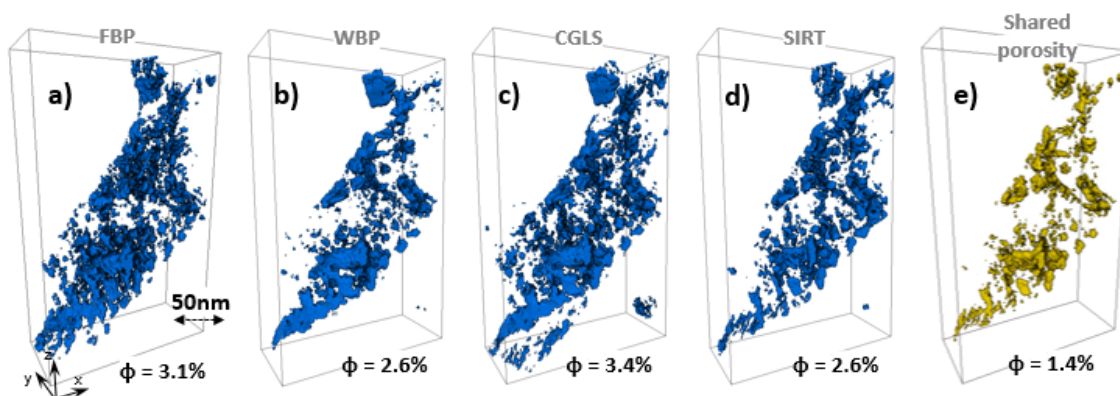


Figure 11. 3D reconstructions of the porosity with different techniques (a: FBP, b: WBP, c: CGLS, d: SIRT). e) Porosity common to all reconstructions.

An analysis of the pore space is presented in Fig. 12. Individual pores are isolated and described using the maximum Feret diameter that is a proxy for pore length. Fig. 12a) shows the increase of the cumulative porosity with pore lengths. Fig. 12b) describes the pore size distribution (PSD). Both figures indicate that, while nanopores between 20 and 80 nm in diameter are limited in number, they contribute significantly to the total porosity and make up to 80% of the total void space. In contrast, there are significantly more pores with diameter below 20 nm, but their void contribution represents less than 20% of the total porosity. We identify small spherical, ellipsoidal shapes, mostly unconnected, as well as tubular, elongated pore channels, some of which are connected across the thin section. Overall, the four reconstructions retrieve similar structures with comparable porosity despite some reconstructions yielding slightly more porosity (CGLS) or appearing more fragmented (FBP).

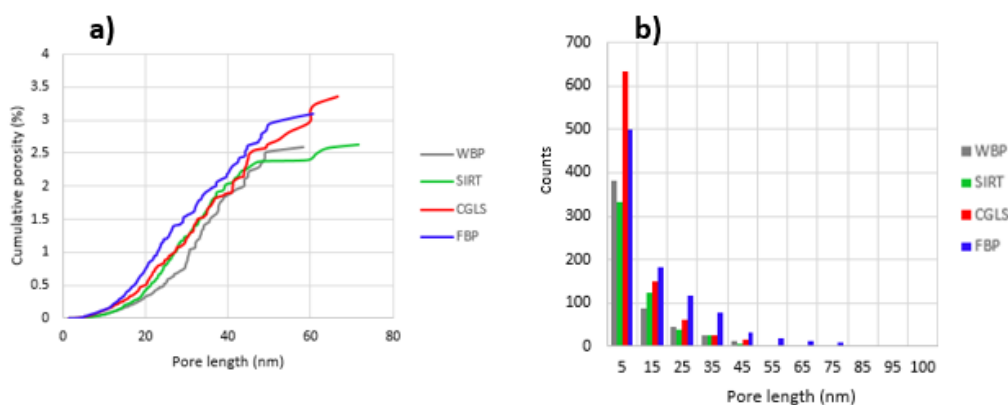


Figure 12. a) Comparison of the cumulative porosity for all reconstructions. b) Pore size distribution (PSD) for all reconstructions.

The four different reconstructions, however, differ more significantly in terms of connectivity. As previously discussed, the image quality is simply not sufficient to resolve properly connected structures below 20 nm in diameter. Therefore, different reconstruction methods disagree on whether the smallest pores are connected, as visible in Fig. 11. In order to study the impact on permeability, we conducted a flow simulation across the XZ planes, in the Y direction. Figure 13 provides an overview of the resulting pressure maps and highlights the active flow paths. Despite the large connectivity differences, absolute permeabilities of 5.3 to 6.5 nD are measured with Darcy's law for the four reconstructed volumes. Fig. 13e) shows that the shared flow pathways across all reconstructions contribute to at least 50% of the total permeability. The other half of the permeability is dependent upon the smallest pore networks, and a variability of up to 20% in total permeability is observed between the different methods.

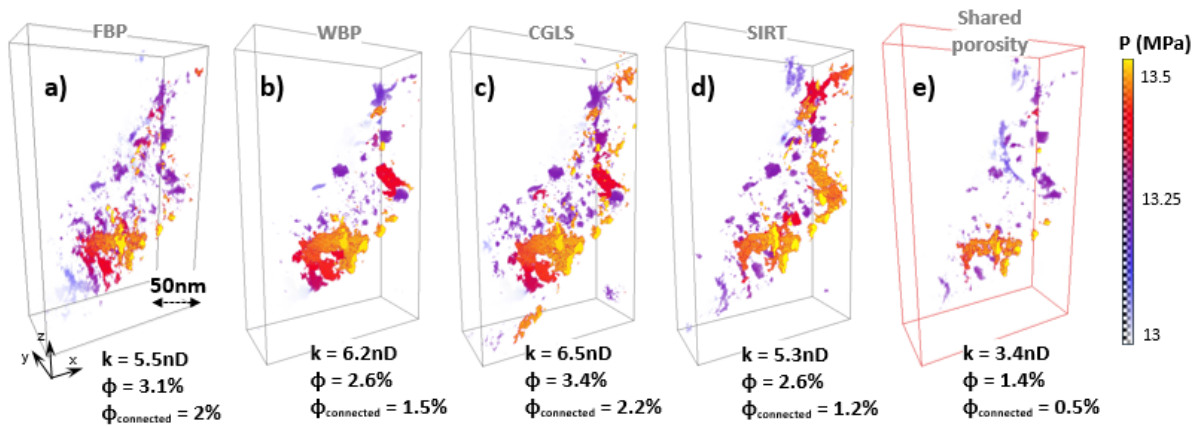


Figure 13. Pressure maps obtained from the flow simulations (a: FBP, b: WBP, c: CGLS, d: SIRT). e) Pressure map of the shared porosity.

Segmentation

Aside from the 3D reconstruction, the user-supervised pixel classification (i.e. segmentation of the voxels corresponding to pores) also inevitably introduces a small amount of variability and bias in the reconstructed 3D structure. That is because the user has to assign manually phases during training. To quantify the variability introduced by user-supervised segmentation, we perform five different segmentations of the same FBP-reconstructed image stack. These are performed by the same researcher, over different days. The pressure maps, given in Fig. 14, show that segmentation bias can result in significant variations. However, despite the variability, a permeability simulation on the shared porosity across segmentations, shown in Fig. 14.f), proves that the main storage and flow features are still captured.

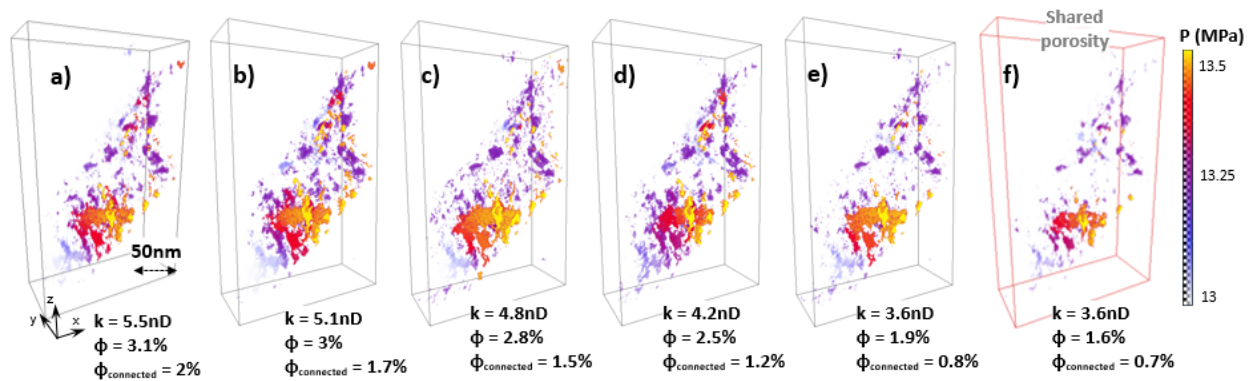


Figure 14. a-e) Pressure maps illustrating the uncertainty of segmentation. f) Pressure map of the shared porosity.

Discussion

Despite its advantageous resolution, ET poses several challenges, including a limited projection range. Single-axis tomography inherently under-samples specimens' structure. This missing wedge of information means features in the beam direction can be stretched by an elongation factor > 1 , leading to anisotropic resolution (Ercius et al., 2015). This is apparent in the reconstruction of gold-shadowed beads performed in this study, and is discussed in multiple publications (Acar et al., 2016; Ercius et al., 2015; Paavolainen et al., 2014). Fundamentally, the missing wedge is caused by a combination of two factors. First, mechanical limitations exist due to the structure of the sample holder and the narrow design of the pole piece of the objective lens. Second, the lamella geometry imposes physical constraints during rotation that result in reduced electron transmission at large angles. Beyond 60° , the beam is transmitted through

twice as much material as at 0° and this material obstructs transmission through the sample. In our case, although the holder is designed for $\pm 70^\circ$ rotation, $\pm 60^\circ$ is the maximum angular range that we can reach because the shale lamella is obscured beyond $\pm 60^\circ$. One possible solution consists of performing double-tilt axis tomography, where sample rotation is performed along two separate tilt axes. However, a double tilt series significantly complicates the post-processing alignment and reconstruction. The use of this technique is not widespread because it is so technically demanding and possibly damages the sample by doubling the electron dosage during acquisition.

HAADF-STEM images measure the intensity of incoherently scattered electrons, but the low flux of highly scattered electrons leads to low electron doses per frame. Therefore, although HAADF-STEM has the benefit of Z-enhanced contrast, it suffers from a limited SNR (Ercius, 2015). Increasing the number of frames is a commonly used technique to increase the electron counts and reduce the noise level (Paavolainen et al., 2014). Unfortunately, acquiring more frames increases the acquisition time and causes the cumulative electron dose to increase and may lead to beam radiation damage of the thin sample. Tilt increments are typically kept at $1\text{--}2^\circ$ in order to preserve the smallest features.

Both the incomplete range (“missing wedge”), and the discrete number of projections (small SNR) introduce errors into the final reconstructions (elongation and blurring). Figure 15 depicts the mean and standard deviation values for porosity and permeability over the multiple tests we performed. It illustrates the uncertainty introduced by the two main limitations of ET. Note that, for both the limited angular range and the small SNR cases, we began with optimal settings ($\pm 60^\circ$, 121 images) and progressively reduced the datasets (down to 41 images). This result highlights that both angle range and SNR are critical to reconstruct properly nanometer scale pore networks.

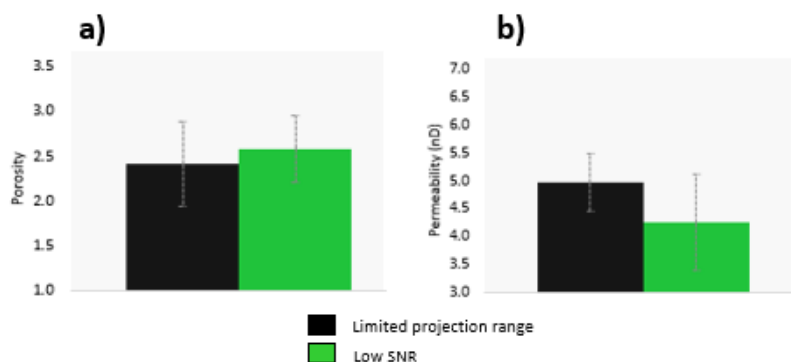


Figure 15. Bar graphs illustrating the uncertainty introduced by limitations in the acquisition modalities: a) porosity and b) permeability.

The present work also addressed the uncertainty of the two main post-acquisition processes: 3D reconstruction and segmentation. We compare 3D shale structures obtained by four standard tomography reconstruction techniques (FBP, WBP, CGLS, SIRT), and compare the outcome of five different segmentation iterations. A strong agreement is found to exist for large pore regions over the different ET reconstruction workflows and segmentations performed, while a wider variability exists for features below 20 nm in diameter. For an acquisition performed at optimal conditions, the reconstructions all lead to similar pore structures, and the main flow paths are commonly captured. Figure 16 illustrates the uncertainty introduced by 3D reconstruction and porosity segmentation by depicting the mean and standard deviation for porosity and permeability over the multiple tests we performed. These results show that reconstruction and segmentation contribute similarly to uncertainty, and that errors of up to 30% can be expected.

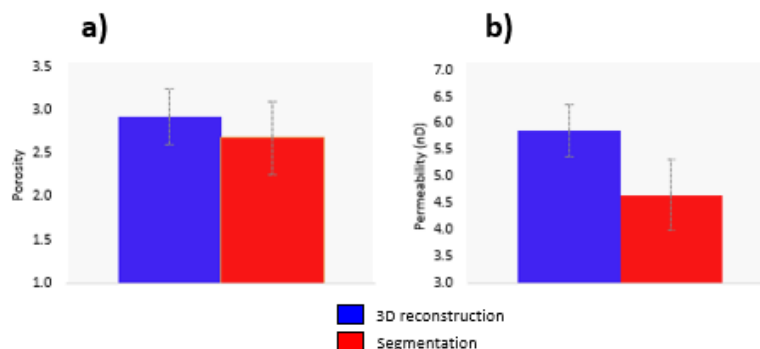


Figure 16. Bar graphs illustrating the uncertainty introduced by post-acquisition treatment: a) porosity and b) permeability.

Conclusions

Today, electron microscopy techniques alone offer the resolution to characterize the morphology, connectivity, and flow properties of shale nanopores. ET imaging in particular provides meaningful contributions in the characterization of shale morphologies, and the development of multiscale tools for the simulation of hydrocarbon transport (Frouté et al., 2020). This study quantitatively evaluated the capabilities of ET for shale applications, and the reliability of produced 3D shale nanostructures. We performed tomographic reconstructions of a Barnett shale dataset, compared storage and transport metrics, and evaluated the challenges imposed by the acquisition modalities as well as by post-acquisition processes. We found that a sensitive balance between angular range, angular increments, and electron dosage was required to achieve sufficient spatial resolution and SNR, while preserving the finest features from electron damage. For the purpose of shale imaging, we found $\pm 60^\circ$ tilt range with 1° increments to be the optimal acquisition settings.

Comparisons of different reconstruction algorithms showed that across methods, ET provides robust estimates of the porosity of shale samples, and good representations of pore structures above 20 nm in diameter. The FBP, WBP, CGLS and SIRT techniques produced similar estimates of the porosity and largest percolating flow paths across the lamella. Our study, however, revealed that describing porous structures below 20 nm in diameter remains challenging, primarily because of missing wedge artifacts, noise limitations, and segmentation repeatability. Specifically, our results suggested that up to 50% of the permeability is due to connected small pore networks, that are only poorly resolved by ET, even with state-of-the-art equipment and methods.

Given the nanometer spatial resolution enabled by HAADF-STEM, however, there is a clear opportunity for improving the fidelity of these diagnostics and better resolution of the nanopores within shale rocks. In particular, promising improvements could come from the mechanical design of the holder and samples to allow tomographic acquisition over a greater angular range. Besides, recent algorithmic efforts to regularize the reconstruction volume or extrapolate the missing angular information represent opportunities to reduce missing-wedge artifacts. Finally, given the image quality, simple segmentation methods are not appropriate, and the segmentation step requires data-based segmentation involving user supervision and inspection. A wide variability in the nano-structure was observed depending on the segmentation training. This result suggests that large uncertainties are still to be expected, and that improvements in ML-based segmentation could largely benefit ET nanoscale imaging. These combined perspectives represent promising opportunities to characterize complex shale nano-structures more reliably and accurately using ET imaging.

Symbols and acronyms

k	permeability
ϕ	porosity
CGLS	conjugate gradient least squares
ET	electron tomography
FBP	filtered back projection
FIB-SEM	focused ion beam scanning electron microscopy
FV	finite volume
HAADF	high-angle annular dark field
ML	machine learning
PSD	pore size distribution
ROI	region of interest
SIRT	simultaneous iterative reconstruction technique
SNR	signal-to-noise ratio
STEM	scanning transmission electron microscopy
WBP	weighted back projection

References

- Acar, E., Peltonen, S., Ruotsalainen, U., 2016. Adaptive multiresolution method for MAP reconstruction in electron tomography. *Ultramicroscopy*, 170, 24-34. <https://doi.org/10.1016/j.ultramic.2016.08.002>
- Adler, P.M., Davy, C.A., Marinova, M., and Mussi, A., 2020. Investigation of the 3D pore structure of a natural shale - implications for mass transport. *E3S Web of Conferences* 205, 08005. <https://doi.org/10.1051/e3sconf/202020508005>
- Bernard, S., Brown, L., Wirth, R., Schreiber, A., Schulz, H.M., Horsfield, B., Aplin, A.C., and Mathia, E.J., 2013. FIB-SEM and TEM Investigations of an Organic-rich Shale Maturation Series from the Lower Toarcian Posidonia Shale, Germany: Nanoscale Pore System and Fluid-rock Interactions. In W. Camp, E. Diaz, and B. Wawak, eds., *Electron microscopy of shale hydrocarbon reservoirs: AAPG Memoir* 102, p. 53–66. <https://doi.org/10.1306/13391705M1023583>
- Berthonneau, J., Obliger, A., Valdenaire, P.L., Grauby, O., Ferry, D., Chaudanson, D., Levitz, P., Kim, J.J., Ulm, F.J., and Pellenq, R.J.M., 2018. Mesoscale structure, mechanics, and transport properties of source rocks' organic pore networks. *PNAS*, 115, 12365-12370. <https://doi.org/10.1073/pnas.1808402115>
- Chen, L., Kang, Q., Pawar, R., He, Y., and Tao, W., 2015. Pore-scale prediction of transport properties in reconstructed nanostructures of organic matter in shales. *Fuel*, 158, 650-658. <https://doi.org/10.1016/j.fuel.2015.06.022>
- Curtis, M.E., Sondergeld, C.H., Ambrose, R.J., and Rai, C.S., 2012. Microstructural investigation of gas shales in two and three dimensions using nanometer-scale resolution imaging. *AAPG Bulletin*, 96, 4, 665-677. <https://doi.org/10.1306/08151110188>
- Ercius, P., Alaidi, O., Rames, M.J. and Ren, G., 2015. Electron Tomography: A Three-Dimensional Analytic Tool for Hard and Soft Materials Research. *Adv. Mater.*, 27: 5638-5663. <https://doi.org/10.1002/adma.201501015>
- Frouté, L., and Kovscek, A.R., 2020. Nano-Imaging of Shale using Electron Microscopy Techniques. Presented at the SPE/AAPG/SEG Unconventional Resources Technology Conference, Virtual, 20-22 July. <https://doi.org/10.15530/urtec-2020-3283>

- Frouté, L., Wang, Y., McKinzie, J., Aryana, S.A., and Kovscek, A.R., 2020. Transport Simulations on Scanning Transmission Electron Microscope Images of Nanoporous Shale. *Energies*, 13, 6665. <https://doi.org/10.3390/en13246665>
- Goral, J., Walton, I., Andrew, M., and Deo, M., 2019. Pore system characterization of organic-rich shales using nanoscale-resolution 3D imaging. *Fuel*, 258, 116049. <https://doi.org/10.1016/j.fuel.2019.116049>
- Guo, B., Ma, L., and Tchalepi, H.A., 2018. Image-based Micro-continuum Model for Gas Flow in Organic-Rich Shale Rock. *Adv Water Resour*, 122, 70-84. <https://doi.org/10.1016/j.advwatres.2018.10.004>
- Loucks, R.G., Reed, R.M., Ruppel, S.C., and Hammes, U., 2012. Spectrum of pore types and networks in mudrocks and a descriptive classification for matrix-related mudrock pores. *AAPG Bulletin*, 96, 6, 1071-1098. <https://doi.org/10.1306/08171111061>
- Ma, L., Slater, T., Dowey, P.J., Yue, S., Rutter, E.H., Taylor, K.G., and Lee, P.D., 2018. Hierarchical integration of porosity in shales. *Sci Rep*, 8, 11683. <https://doi.org/10.1038/s41598-018-30153-x>
- Messaoudil, C., Boudier, T., Sanchez Sorzano, C.O., Marco, S., 2007. TomoJ: tomography software for three-dimensional reconstruction in transmission electron microscopy. *BMC Bioinformatics*, 8:288. <https://doi.org/10.1186/1471-2105-8-288>
- Paavolainen, L., Acar, E., Tuna, U., Peltonen, S., Moriya, T., Soonsawad, P., Marjomäki, V., Cheng, R.H., and Ruotsalainen, U., 2014. Compensation of missing wedge effects with sequential statistical reconstruction in electron tomography. *PLoS One*, 10. <https://doi.org/10.1371/journal.pone.0108978>
- Penczek, P.A., 2010. Fundamentals of three-dimensional reconstruction from projections. *Meth. Enz.*, 1-33.
- Striolo, A., and Cole, D.R., 2017. Understanding Shale Gas: Recent Progress and Remaining Challenges. *Energy Fuels*, 31, 10300-10310. <https://doi.org/10.1021/acs.energyfuels.7b01023>
- Van Aarle, W., Palenstijn, W. J., Cant, J., Janssens, E., Bleichrodt F., Dabrovolski, A., De Beenhouwer, J., Batenburg, K. J., and Sijbers, J., 2016. Fast and Flexible X-ray Tomography Using the ASTRA Toolbox, *Optics Express*, 24 (22), 25129-25147. <http://dx.doi.org/10.1364/OE.24.025129>
- Zhou, S., Yan, G., Xue, H., Guo, W., and Li, X., 2016. 2D and 3D nanopore characterization of gas shale in Longmaxi formation based on FIB-SEM. *Marine and Petroleum Geology*, 73, 174-180. <https://doi.org/10.1016/j.marpetgeo.2016.02.033>

Acknowledgements

LF acknowledges TOTAL S.A. for financial support. This work was supported as part of the Center for Mechanistic Control of Unconventional Formations (CMC-UF), an Energy Frontier Research Center funded by the U.S. Department of Energy (DOE), Office of Science, Basic Energy Sciences (BES), under Award # DE-SC0019165. Experimental results were obtained in the SNSF facilities at Stanford, supported by the National Science Foundation as part of the National Nanotechnology Coordinated Infrastructure under award ECCS-2026822. We thank Isabelle C. Jolivet (TOTAL S.A.) and Patrice Creux (University of Pau) for helpful discussions related to this study. We are also thankful to Hye Ryoung Lee (Stanford University) for her help in acquiring a tomogram of the phantom.